Supplementary figures and tables for "*Monte Carlo Drift Correction – Quantifying the Drift Uncertainty of Global Climate Models*"

Benjamin S. Grandey[1], Zhi Yang Koh[1], Dhrubajyoti Samanta[2], Benjamin P. Horton[2,3], Justin Dauwels[4], and Lock Yue Chew[1]

[1]School of Physical and Mathematical Sciences, Nanyang Technological University, Singapore
[2]Earth Observatory of Singapore, Nanyang Technological University, Singapore
[3]Asian School of the Environment, Nanyang Technological University, Singapore
[4]Department of Microelectronics, Faculty of Electrical Engineering, Mathematics, and Computer Science, Delft University of Technology (TU Delft), The Netherlands

[Compiled on February 13, 2023.]

This supplement contains eight supplementary figures (Figs. S1–S8) and two supplementary tables (Tables S1–S2).

Further details can be found in the manuscript titled "*Monte Carlo Drift Correction – Quantifying the Drift Uncertainty of Global Climate Models*".

Code availability: The code used to produce these figures and tables is available at https://doi.org/10.5281/zenodo.7488335.

Acknowledgements: This Research/Project is supported by the National Research Foundation, Singapore, and National Environment Agency, Singapore under the National Sea Level Programme Funding Initiative (Award No. USS-IF-2020-3). We acknowledge the World Climate Research Programme, which, through its Working Group on Coupled Modelling, coordinated and promoted CMIP6. We thank the climate modeling groups for producing and making available their model output, the Earth System Grid Federation (ESGF) for archiving the data and providing access, and the multiple funding agencies who support CMIP6 and ESGF.

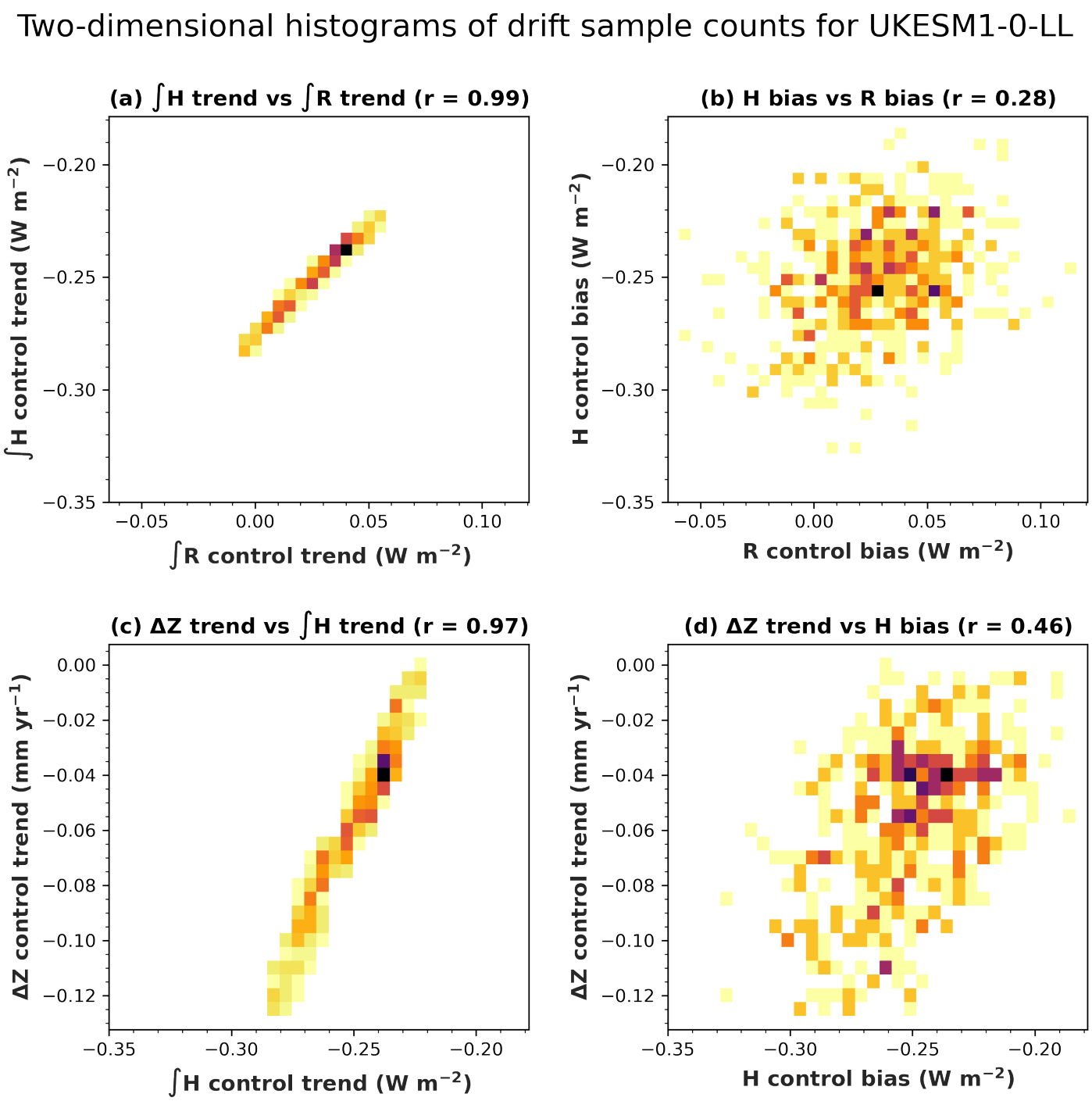

Figure S1: Two-dimensional histograms of drift samples for different variables, revealing dependence. The drift samples are derived from the control simulation of the U.K. Earth System Model (UKESM1). (a) Excess ocean heat ($\int H$) trend samples versus excess system energy ($\int R$) trend samples. These trend samples correspond to the drift samples from trend-method MCDC (Sect. 3.2). (b) Sea-surface heat flux (H) bias samples versus top-of-atmosphere radiative flux (R) bias estimates. These bias samples correspond to the drift samples from integrated-bias-method MCDC (Sect. 3.3). (c) Thermosteric sea-level rise (ΔZ) trend samples versus $\int H$ trend samples. (d) ΔZ trend samples versus H bias samples. The colour map is a perceptually uniform sequential cmap, with darker colours indicating higher counts. The title of each panel contains the Pearson correlation coefficient (r).

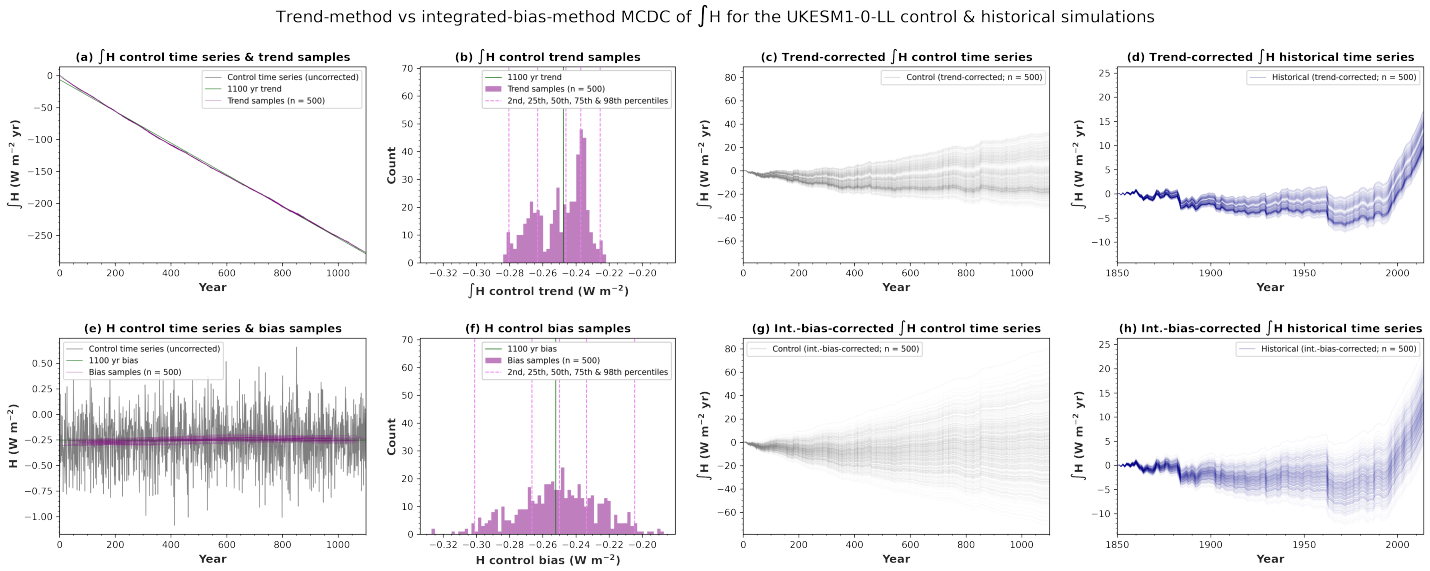

Figure S2: Integrated-bias-method MCDC (second row) compared with trend-method MCDC (first row), applied to excess ocean heat ($\int H$). The first row (a–d) shows trend-method MCDC results. (a) Five hundred trend samples are produced by sampling 500 150 yr segments of the $\int H$ control time series. (b) The trend samples are displayed as a histogram. (c) Each trend sample is subtracted from the uncorrected $\int H$ control time series, producing 500 trend-corrected control time series. (d) Each trend sample (derived from the $\int H$ control time series) is also subtracted from the uncorrected $\int H$ historical time series, producing 500 trend-corrected historical time series. The second row (e–h) shows integrated-bias-method MCDC results. (e) Five hundred bias samples are produced by sampling 500 150 yr segments of the control time series of sea-surface heat flux (H). (f) The bias samples are displayed as a histogram. (g) Each bias sample is subtracted from the uncorrected H control time series, before integrating the bias-corrected H control time series cumulatively to produce 500 integrated-bias-corrected $\int H$ control time series. (h) Each bias sample (derived from the H control time series) is also subtracted from the uncorrected H historical time series, before integrating cumulatively to produce 500 integrated-bias-corrected $\int H$ historical time series.

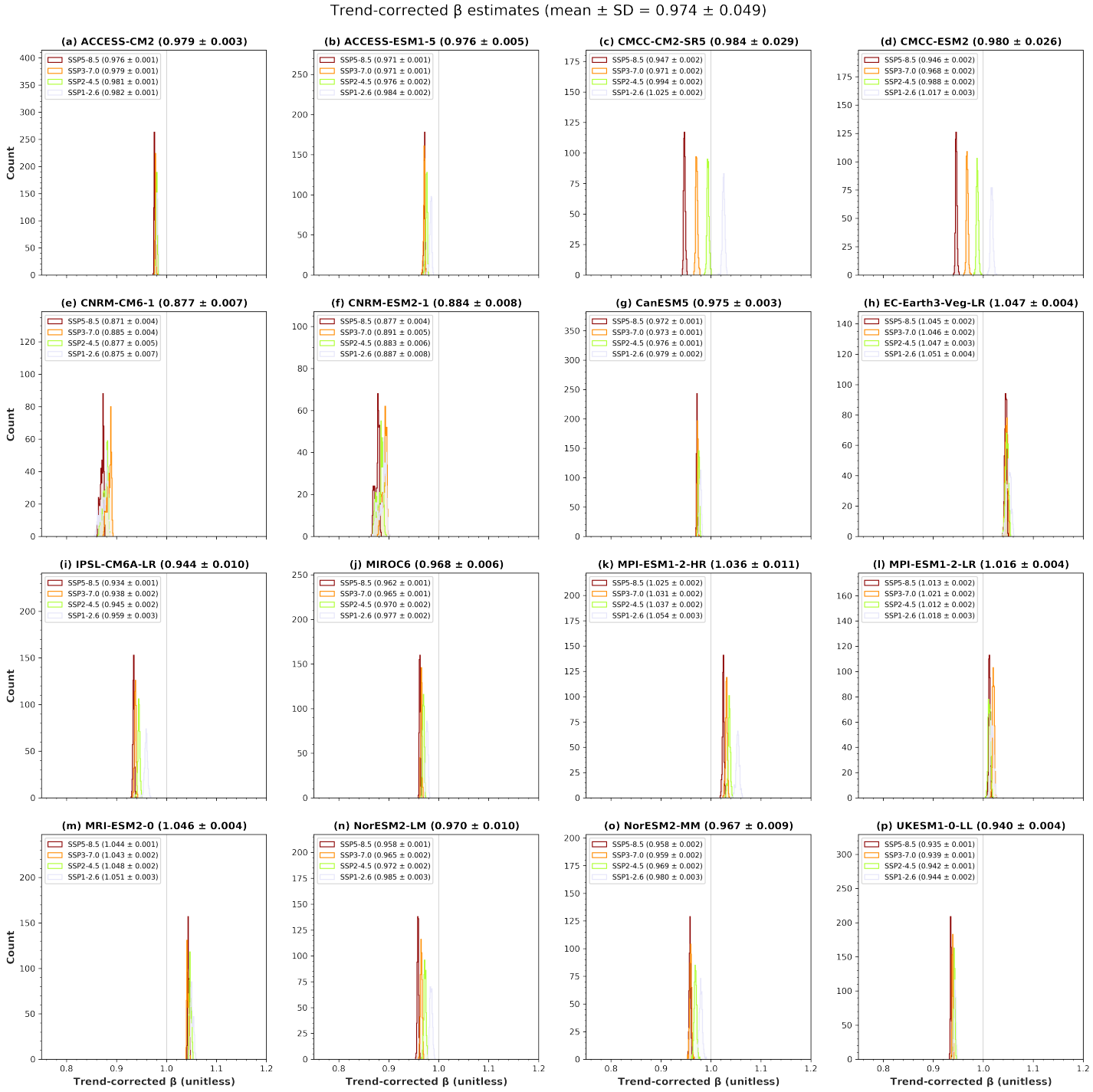

Figure S3: Trend-corrected estimates of the fraction of excess energy absorbed by the ocean (β). Trend-corrected β is calculated as the linear regression coefficient of trend-corrected $\int H$ versus trend-corrected $\int R$ (Appendix B). Each panel shows β estimates for a different CMIP6 model (Table S1). A vertical line at $\beta = 1.0$ shows the theoretical maximum value of β. Means and standard deviations (*not* standard errors) are shown in the legends (for each simulation), in the panel titles (for each model), and in the main title (for the ensemble).

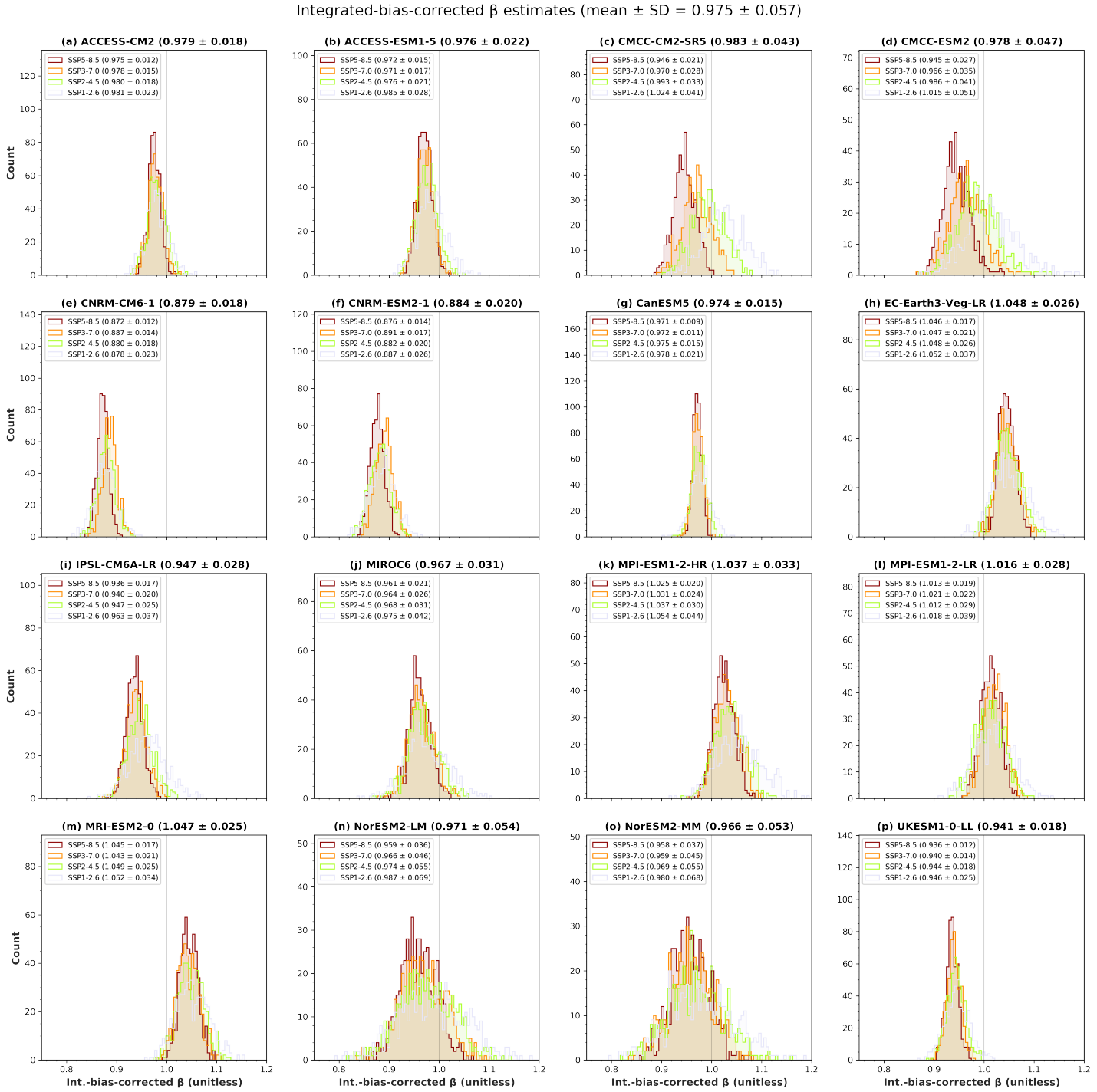

Figure S4: Integrated-bias-corrected estimates of the fraction of excess energy absorbed by the ocean (β). Integrated-bias-corrected β is calculated as the linear regression coefficient of integrated-bias-corrected $\int H$ versus integrated-bias-corrected $\int R$. Each panel shows β estimates for a different CMIP6 model. A vertical line at $\beta = 1.0$ shows the theoretical maximum value of β. Means and standard deviations are shown in the legends, in the panel titles, and in the main title.

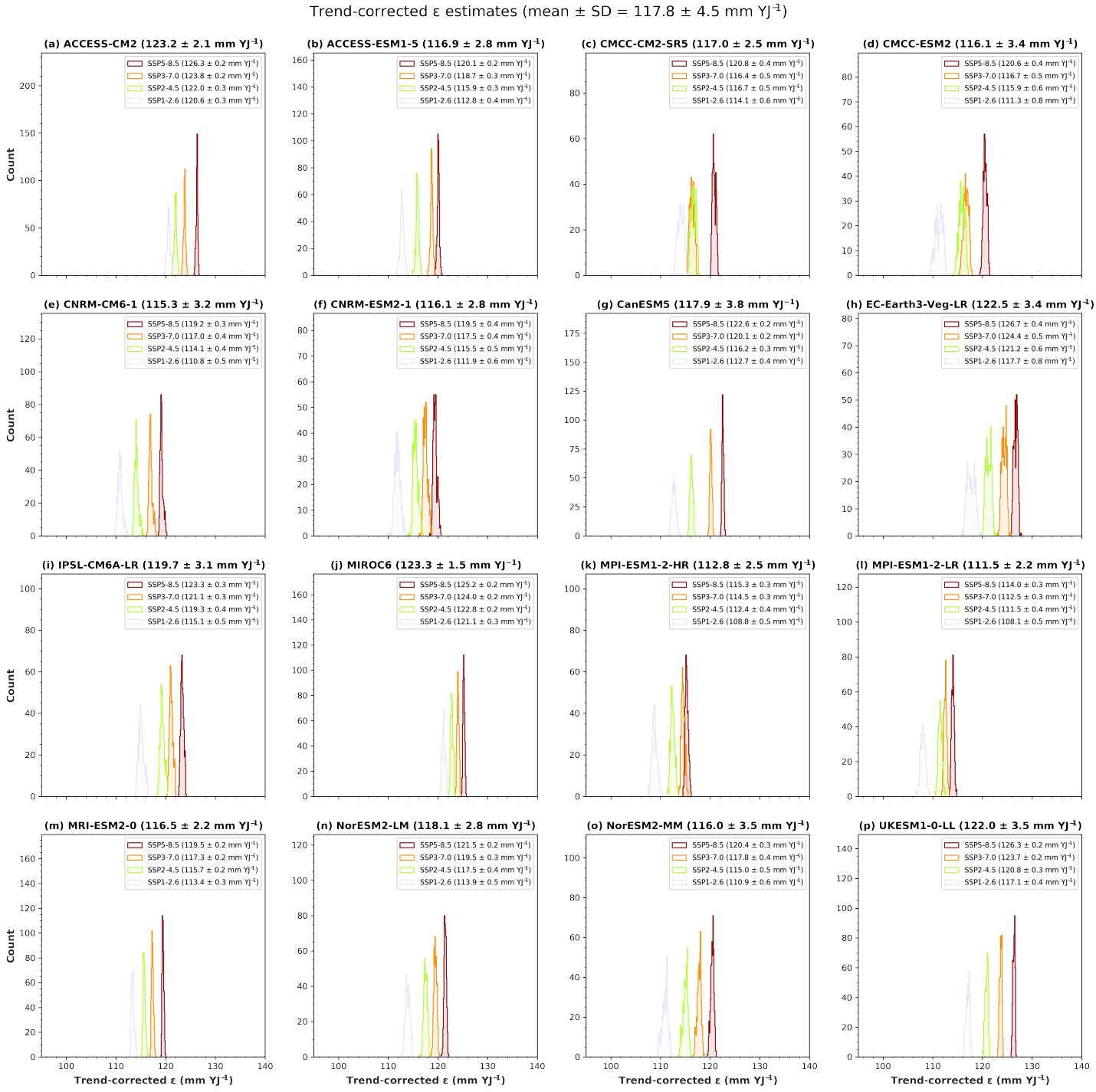

Figure S5: Trend-corrected estimates of the expansion efficiency of heat (ϵ). Trend-corrected ϵ is calculated as the linear regression coefficient of trend-corrected ΔZ versus trend-corrected $\int H$ (Appendix B). Each panel shows ϵ estimates for a different CMIP6 model. Means and standard deviations are shown in the legends, in the panel titles, and in the main title.

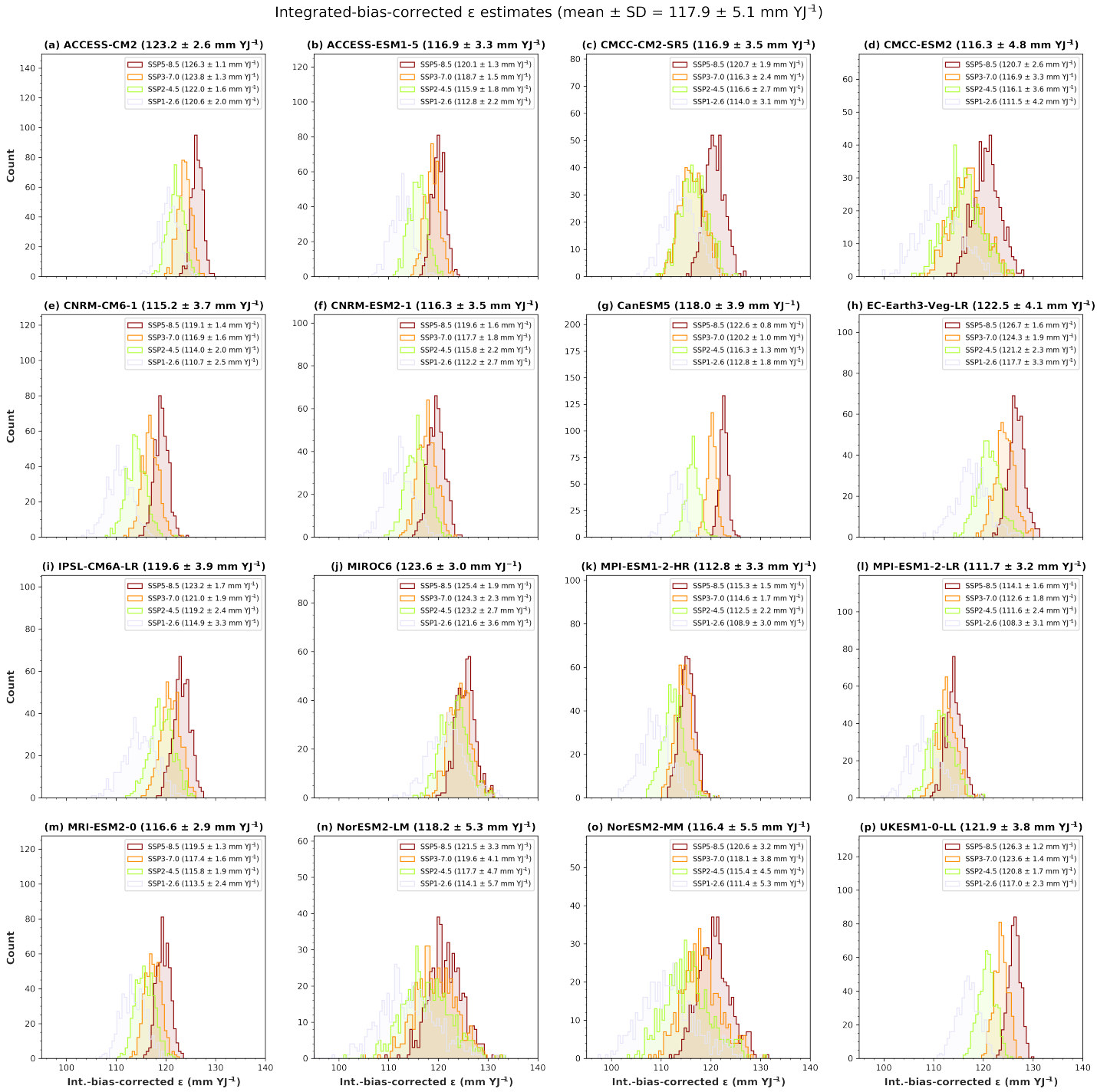

Figure S6: Integrated-bias-corrected estimates of the expansion efficiency of heat (ϵ). Integrated-bias-corrected ϵ is calculated as the linear regression coefficient of trend-corrected ΔZ versus integrated-bias-corrected $\int H$. Each panel shows ϵ estimates for a different CMIP6 model. Means and standard deviations are shown in the legends, in the panel titles, and in the main title.

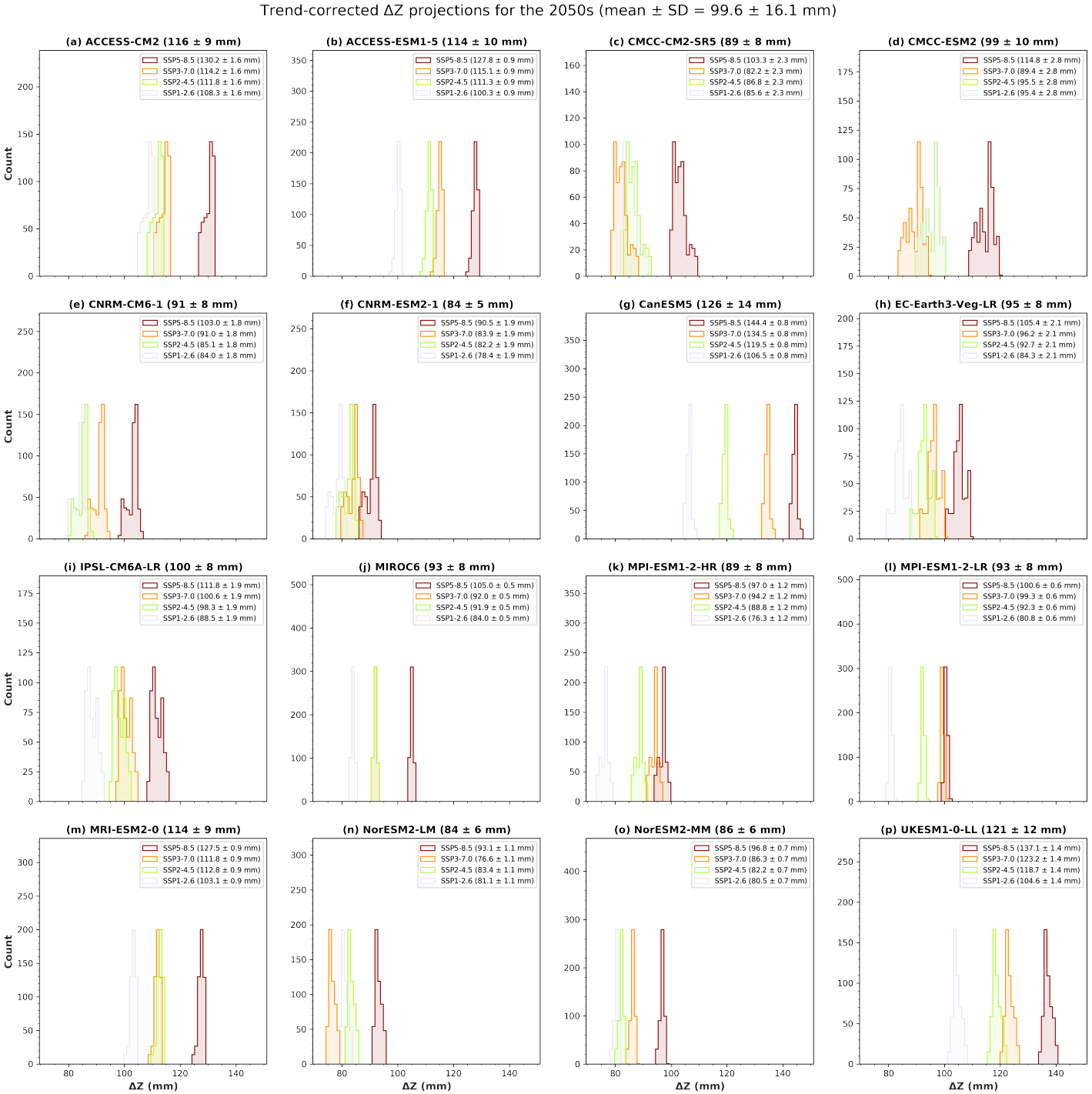

Figure S7: Trend-corrected thermosteric sea-level rise (ΔZ) averaged across 2050–2059. Results are shown relative to 1995–2014. Each panel shows ΔZ for a different CMIP6 model. Means and standard deviations are shown in the legends, in the panel titles, and in the main title.

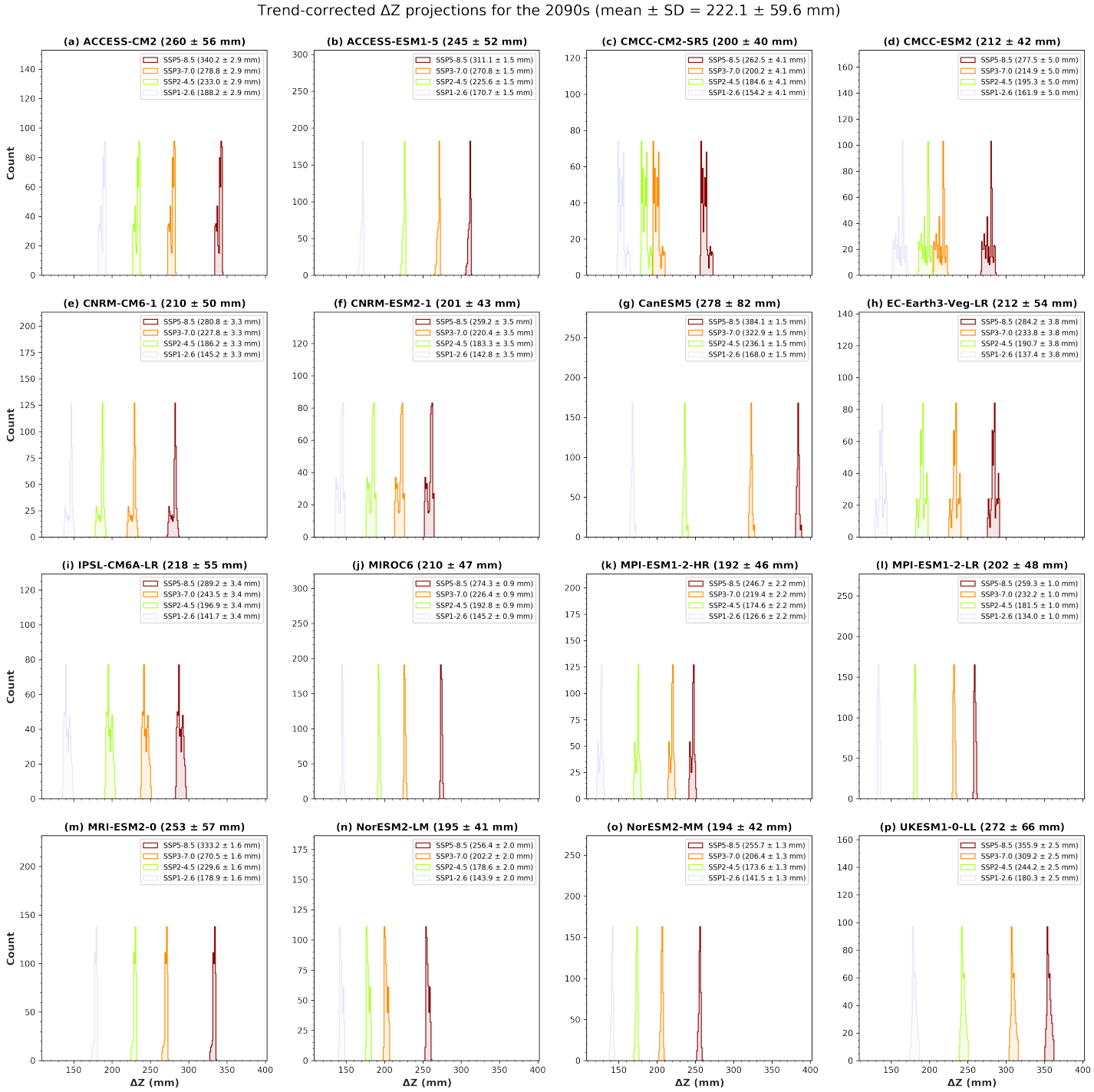

Figure S8: Trend-corrected thermosteric sea-level rise (ΔZ) averaged across 2090–2099. Results are shown relative to 1995–2014. Each panel shows ΔZ for a different CMIP6 model. Means and standard deviations are shown in the legends, in the panel titles, and in the main title.

Table S1: Coupled Model Intercomparison Project Phase 6 (CMIP6) models analysed in this study. "Control length" refers to the time series length of the pre-industrial control simulation data. The further information URLs also correspond to the control simulations. The calendar information influences ϵ via the conversion factor between W m^{-2} yr and YJ.

Model	Variant	Control length (yr)	Calendar	Further information URL
ACCESS-CM2	r1i1p1f1	500	proleptic gregorian	https://furtherinfo.es-doc.org/CMIP6.CSIRO-ARCCSS.ACCESS-CM2.piControl.none.r1i1p1f1
ACCESS-ESM1-5	r1i1p1f1	1000	proleptic gregorian	https://furtherinfo.es-doc.org/CMIP6.CSIRO.ACCESS-ESM1-5.piControl.none.r1i1p1f1
CMCC-CM2-SR5	r1i1p1f1	500	365 day	https://furtherinfo.es-doc.org/CMIP6.CMCC.CMCC-CM2-SR5.piControl.none.r1i1p1f1
CMCC-ESM2	r1i1p1f1	500	365 day	https://furtherinfo.es-doc.org/CMIP6.CMCC.CMCC-ESM2.piControl.none.r1i1p1f1
CNRM-CM6-1	r1i1p1f2	500	gregorian	https://furtherinfo.es-doc.org/CMIP6.CNRM-CERFACS.CNRM-CM6-1.piControl.none.r1i1p1f2
CNRM-ESM2-1	r1i1p1f2	500	gregorian	https://furtherinfo.es-doc.org/CMIP6.CNRM-CERFACS.CNRM-ESM2-1.piControl.none.r1i1p1f2
CanESM5	r1i1p1f1	1000	365 day	https://furtherinfo.es-doc.org/CMIP6.CCCma.CanESM5.piControl.none.r1i1p1f1
EC-Earth3-Veg-LR	r1i1p1f1	501	proleptic gregorian	https://furtherinfo.es-doc.org/CMIP6.EC-Earth-Consortium.EC-Earth3-Veg-LR.piControl.none.r1i1p1f1
IPSL-CM6A-LR	r1i1p1f1	1000	gregorian	https://furtherinfo.es-doc.org/CMIP6.IPSL.IPSL-CM6A-LR.piControl.none.r1i1p1f1
MIROC6	r1i1p1f1	500	gregorian	https://furtherinfo.es-doc.org/CMIP6.MIROC.MIROC6.piControl.none.r1i1p1f1
MPI-ESM1-2-HR	r1i1p1f1	500	proleptic gregorian	https://furtherinfo.es-doc.org/CMIP6.MPI-M.MPI-ESM1-2-HR.piControl.none.r1i1p1f1
MPI-ESM1-2-LR	r1i1p1f1	1000	proleptic gregorian	https://furtherinfo.es-doc.org/CMIP6.MPI-M.MPI-ESM1-2-LR.piControl.none.r1i1p1f1
MRI-ESM2-0	r1i1p1f1	701	proleptic gregorian	https://furtherinfo.es-doc.org/CMIP6.MRI.MRI-ESM2-0.piControl.none.r1i1p1f1
NorESM2-LM	r1i1p1f1	501	365 day	https://furtherinfo.es-doc.org/CMIP6.NCC.NorESM2-LM.piControl.none.r1i1p1f1
NorESM2-MM	r1i1p1f1	500	365 day	https://furtherinfo.es-doc.org/CMIP6.NCC.NorESM2-MM.piControl.none.r1i1p1f1
UKESM1-0-LL	r1i1p1f2	1100	360 day	https://furtherinfo.es-doc.org/CMIP6.MOHC.UKESM1-0-LL.piControl.none.r1i1p1f2

Table S2: Sources of uncertainty in β (fraction of excess energy absorbed by the ocean), ϵ (expansion efficiency of heat), and ΔZ (thermosteric sea-level rise, relative to 1995–2014). For each model, *drift uncertainty* is derived from the 2nd–98th inter-percentile range: (i) for each scenario, calculate the 2nd–98th inter-percentile range of the drift-corrected data, then (ii) calculate the mean of this inter-percentile range by averaging across the scenarios. For each model, *scenario uncertainty* is derived from the inter-scenario range: (i) for each scenario, calculate the mean of the drift-corrected data, then (ii) calculate the inter-scenario range. For each scenario, *model uncertainty* is derived from the inter-model range: (i) for each model, calculate the mean of the drift-corrected data, then (ii) calculate the inter-model range. For β and ϵ, drift uncertainty is calculated using both trend-method MCDC and integrated-bias-method MCDC. Scenario uncertainty and model uncertainty are relatively insensitive to the choice of drift correction method, so these sources of uncertainty are shown for trend-method MCDC only. When calculating the uncertainty in β, ϵ, and ΔZ for future decades, the four projection scenarios are used (but not the historical scenario). When calculating the uncertainty in ΔZ for the 1850s, the single historical scenario is used instead, hence scenario uncertainty cannot be calculated for the 1850s. The values in Table 1 of the main manuscript have been calculated by averaging across all models or scenarios for each source of uncertainty.

Source of uncertainty	Model or scenario	Uncertainty in β (unitless)		Uncertainty in ϵ (mm YJ^{-1})		Uncertainty in ΔZ (mm)		
		Trend-method	Int.-bias-method	Trend-method	Int.-bias-method	1850s	2050s	2090s
Drift uncertainty	ACCESS-CM2	0.00	0.07	1.0	5.9	15	5	9
	ACCESS-ESM1-5	0.01	0.08	1.3	6.9	10	3	6
	CMCC-CM2-SR5	0.01	0.12	1.7	10.0	25	8	15
	CMCC-ESM2	0.01	0.15	2.1	13.6	29	10	17
	CNRM-CM6-1	0.02	0.07	1.5	7.5	20	7	12
	CNRM-ESM2-1	0.02	0.08	1.8	8.5	20	7	12
	CanESM5	0.00	0.06	1.0	5.3	11	4	6
	EC-Earth3-Veg-LR	0.01	0.11	2.0	9.5	24	8	14
	IPSL-CM6A-LR	0.01	0.10	1.6	9.5	20	7	12
	MIROC6	0.01	0.13	0.9	10.7	6	2	3
	MPI-ESM1-2-HR	0.01	0.11	1.5	8.3	14	5	8
	MPI-ESM1-2-LR	0.01	0.11	1.4	9.0	6	2	4
	MRI-ESM2-0	0.01	0.10	0.9	7.0	11	4	6
	NorESM2-LM	0.01	0.22	1.3	18.3	11	4	7
	NorESM2-MM	0.01	0.20	1.8	17.3	9	3	5
	UKESM1-0-LL	0.01	0.07	1.0	6.4	17	6	10
Scenario uncertainty	ACCESS-CM2	0.01		5.7			22	152
	ACCESS-ESM1-5	0.01		7.3			28	140
	CMCC-CM2-SR5	0.08		6.7			21	108
	CMCC-ESM2	0.07		9.3			25	116
	CNRM-CM6-1	0.01		8.4			19	136
	CNRM-ESM2-1	0.01		7.6			12	116
	CanESM5	0.01		9.8			38	216
	EC-Earth3-Veg-LR	0.01		9.0			21	147
	IPSL-CM6A-LR	0.02		8.3			23	148
	MIROC6	0.01		4.1			21	129
	MPI-ESM1-2-HR	0.03		6.5			21	120
	MPI-ESM1-2-LR	0.01		6.0			20	125
	MRI-ESM2-0	0.01		6.1			24	154
	NorESM2-LM	0.03		7.6			17	113
	NorESM2-MM	0.02		9.5			16	114
	UKESM1-0-LL	0.01		9.3			33	176
Model uncertainty	Historical					69		
	SSP1-2.6	0.18		13.1			32	62
	SSP2-4.5	0.17		11.3			37	71
	SSP3-7.0	0.16		11.8			58	123
	SSP5-8.5	0.17		12.7			54	137